The Astrophysical Journal, 817:15 (16pp), 2016 January 20 doi:10.3847/0004-637X/817/1/15

A THREE-DIMENSIONAL MODEL OF ACTIVE REGION 7986: COMPARISON OF SIMULATIONS WITH OBSERVATIONS

Yung Mok[1], Zoran Mikić[2], Roberto Lionello[2], Cooper Downs[2], and Jon A. Linker[2]
[1] Department of Physics and Astronomy, University of California, Irvine, CA 92697, USA; ymok@uci.edu
[2] Predictive Science, Inc., San Diego, CA 92121, USA
Received 2015 April 10; accepted 2015 November 24; published 2016 January 19

ABSTRACT

In the present study, we use a forward modeling method to construct a 3D thermal structure encompassing active region 7986 of 1996 August. The extreme ultraviolet (EUV) emissions are then computed and compared with observations. The heating mechanism is inspired by a theory on Alfvén wave turbulence dissipation. The magnetic structure is built from a *Solar and Heliospheric Observatory* (*SOHO*)/MDI magnetogram and an estimated torsion parameter deduced from observations. We found that the solution to the equations in some locations is in a thermal nonequilibrium state. The time variation of the density and temperature profiles leads to time dependent emissions, which appear as thin, loop-like structures with uniform cross-section. Their timescale is consistent with the lifetime of observed coronal loops. The dynamic nature of the solution also leads to plasma flows that resemble observed coronal rain. The computed EUV emissions from the coronal part of the fan loops and the high loops compare favorably with *SOHO*/EIT observations in a quantitative comparison. However, the computed emission from the lower atmosphere is excessive compared to observations, a symptom common to many models. Some factors for this discrepancy are suggested, including the use of coronal abundances to compute the emissions and the neglect of atmospheric opacity effects.

Key words: Sun: atmosphere – Sun: corona – Sun: UV radiation

Supporting material: animations

1. INTRODUCTION

Radiative signatures from active regions on the Sun have been observed for many years, most frequently in extreme ultraviolet (EUV) and soft X-rays. In principle, these observations can be used to infer the plasma density and temperature in these regions, and to constrain the possible mechanisms that heat the corona to millions of degrees. Early observation of loop-like structures, such as those seen in *Skylab* X-ray images, together with the known high coronal temperatures and strong solar magnetic field, naturally led to the idea that these loops outlined closed magnetic flux tubes containing hot coronal plasma. In this context, the high thermal conductivity of the coronal plasma leads to the compelling assumption that these loops can be treated with one-dimensional models (Craig et al. 1978; Rosner et al. 1978; Hood & Priest 1979; Vesecky et al. 1979; Serio et al. 1981). The success of the Rosner et al. (1978) scaling laws in explaining *Skylab* X-ray observations validated this approach, and these 1D computational models of coronal loops have led to further insights. Subsequent EUV observations of "warm" (∼1 MK) loops from the *Solar and Heliospheric Observatory* (*SOHO*)/EIT and *TRACE* (Lenz et al. 1999) were found to be incompatible with steady-state models (Klimchuk 2006).

One possible explanation that emerged to explain the detailed, non-steady properties of coronal loops are the so-called "nanoflare storms" (Klimchuk 2009). In this idea, coronal loops consist of bundles of unresolved strands that are impulsively heated intermittently and then evolve independently from their neighbors. The sum of the emission from these strands then define the emission properties of the loop. However, it is important to note that non-steady heating is not required to obtain non-steady behavior in coronal loops. Rosner et al. (1978) recognized that if the heating in a coronal loop is localized near its footpoints on a short enough length scale, the equations do not admit steady-state solutions, even for steady heating. Concentrated footpoint heating yields solutions that can repetitively oscillate in time through condensation–evaporation cycles, in which material begins to condense suddenly at the top of the loop, falls down the loop legs, and is followed by evaporation of material from the chromosphere, filling the loop with hot plasma. This unstable behavior has been called "thermal nonequilibrium" (Kuin & Martens 1982; Martens & Kuin 1983; Antiochos & Klimchuk 1991; Antiochos et al. 1999, 2000; Müller et al. 2003, 2004; Karpen et al. 2005, 2006; Xia et al. 2011; Peter et al. 2012), and is believed to manifest itself as "coronal rain" in observations (De Groof et al. 2004, 2005; Müller et al. 2005; Antolin et al. 2010; Antolin & Rouppe van der Voort 2012; Ahn et al. 2014; Antolin et al. 2015). In the past, these results were not recognized as being applicable to loops observed in EUV at warm temperatures.

While 1D models are useful for understanding the basic physics of loops, it is difficult to compare the solutions directly with observations, which result from the convolution of plasma properties in many loops, integrated along the line of sight. In the "forward modeling" approach, full three-dimensional models (Gudiksen & Nordlund 2005a, 2005b; Mok et al. 2005, 2008; Hansteen et al. 2007; Carlsson et al. 2010; Bingert & Peter 2011; Peter & Bingert 2013) allow the development of simulated emission in the same manner as the observations. This has also been attempted using a multitude of 1D loop solutions simultaneously (Lundquist et al. 2004, 2008a, 2008b; Brooks & Warren 2006; Warren & Winebarger 2006). Luna et al. (2012) extracted field lines from a computed 3D AR magnetic structure, and subsequently conducted 1D thermodynamic simulations along these field lines.

Mok et al. (2008), using three-dimensional simulations of active region AR 7986, observed in 1996 August, found that thermal nonequilibrium naturally occurred when the AR was sufficiently heated to match the X-ray emission observed by *Yohkoh*/SXT. They found that the model gave rise to thin coronal loops with qualitative features similar to observed loops. In particular, the EUV emission was much stronger than in hydrostatic solutions, in agreement with observations of "overdense" loops (Winebarger et al. 2003; Klimchuk 2006). However, Klimchuk et al. (2010) summarized five observational properties of coronal loops that must be successfully reproduced by a viable model. Based on idealized, 1D simulations, they argued that thermal nonequilibrium was not compatible with these observational tests.

The present paper is the fourth in a series of papers investigating the properties of thermal nonequilibrium in the context of active region loops. The observational tests proposed by Klimchuk et al. (2010) form a useful framework for testing the viability of this mechanism. In paper I, Mikić et al. (2013) showed that the conclusions of Klimchuk et al. (2010) about thermal nonequilibrium were based on the choice of a very narrow range of idealized parameters (perfectly symmetric loops with uniform cross-section and symmetric heating). When more realistic parameters are chosen, 1D solutions consistent with the observational constraints are obtained. Using the same 3D active-region simulation as described in this paper, Lionello et al. (2013) (paper II) investigated the generic properties of the simulated loops and found that they were consistent with the requirements outlined by Klimchuk et al. (2010). In paper III, Winebarger et al. (2014) used this same simulation to investigate how well standard observational techniques can be used to infer the fundamental properties of loops.

One of the advantages of simulating a real active region is that the results can be compared with specific observations, not just generic ones. While this is an obvious approach, it has not been attempted frequently, in part because so many details of the model must be correct for a useful comparison. In this paper (IV), we compare our results with *SOHO*/EIT and *Yohkoh*/SXT observations for AR 7986. We show that the model can provide reasonable quantitative comparisons with the data, but that there are also important discrepancies that may indicate some limitations to the present physical model of emission, and perhaps also our models of coronal heating.

In Section 2, we describe our approach to modeling AR 7986; Section 3 describes our comparison of the simulated emission with observations. Section 4 shows how the underlying thermal structure in the model gives rise to the simulated emission, and in Section 5 we discuss the significance of our results and our conclusions.

2. MODEL AND TECHNICAL APPROACH

We use a forward modeling approach by first establishing a thermal structure in the AR to be studied. EUV emissivity is then computed from the 3D profiles of density and temperature. Finally, line of sight integration is performed from the view angle of the observer to obtain simulated images that can be compared with observations both qualitatively and quantitatively. The basic assumptions of the model, the equations, and the general procedure of this method have already been described in our previous papers (Mok et al. 2005, 2008; Lionello et al. 2013). We choose a sample active region, AR 7986, observed in 1996 August, to demonstrate this technique, although it is applicable to other ARs. Extensive analysis of this AR can be found in the literature (Aschwanden et al. 1999, 2000). Vector magnetograms of sufficiently good quality are unfortunately not available. Therefore, we build a 3D nonlinear force-free structure with an alternative method. A *SOHO*/MDI disk magnetogram on 1996 August 30, at 00:04 UT is used to specify the normal component of the magnetic field at the base. The analysis of the geometry of the *Yohkoh*/SXT soft X-ray loops by Démoulin et al. (2003) provides the approximate torsion parameters (i.e., magnetic field twist). We note that it can be very difficult to reconstruct the field topology correctly even when vector magnetograms are available (Schrijver et al. 2006). Therefore, we must be content with an approximate solution and accept that the geometry of the loops may not agree perfectly with observations. The magnetogram and some of the field lines are shown in Figure 1. A variable-sized (x, y, z) mesh of $359 \times 263 \times 191$ points is used to simulate a volume of dimension $1R_\odot \times 1R_\odot \times 1R_\odot$, with z being the vertical direction. The mesh points are concentrated in the core of the AR and in the chromosphere and lower corona. In the core of the domain, where the active region is located, the mesh spacing in the horizontal plane is 770 km. The vertical mesh spacing is 140 km in the transition region, increasing gradually to 580 km at $z = 25$ Mm, 1100 km at $z = 50$ Mm, and 3100 km at $z = 100$ Mm. We were able to achieve a significantly higher spatial resolution here than in the work described by Mok et al. (2005, 2008) due to improvements in computer speed since our earlier work. In Section 5 we discuss the differences between this work and our previous work more extensively.

The most model-specific element that affects the thermal structure is plasma heating. In contrast with our previous work, we choose a new heating model (Lionello et al. 2013) that is inspired by the Alfvén turbulence dissipation model of Rappazzo et al. (2007, 2008). The chosen volumetric heating rate H depends on a combination of three parameters, the magnetic field strength B, the length of field lines L, and plasma density ρ, namely, $H = H_0 B^a L^b \rho^c$, where the parameters a, b, and c depend on the characteristics of the turbulence. Here, we use $a = 7/4$, $b = -3/4$, and $c = 1/8$. Since L is not a local quantity in the approximation made by Rappazzo et al. (2007, 2008), we replace it with the local radius of curvature of the field line that passes through the point in question, so that H becomes a volumetric heating rate that can be computed locally at each point in space. Although we use the formula of Rappazzo et al. (2007) as given, this model is only a crude approximation because their theory is based on reduced MHD in a "straight" coronal loop of uniform density. The parametric dependence of H on B, ρ and L is not to be taken too literally; other heating models with similar properties will likely produce results with similar characteristics. The constant of proportionality H_0 is chosen empirically to make the brightness of the emitted soft X-rays comparable to *Yohkoh*/SXT observations. For the radiative energy loss, we use a model based on the CHIANTI atomic database (Dere et al. 1997, 2009) with coronal abundances. The radiative energy loss as a function of temperature is shown in Figure 2. Parallel thermal conduction is based on the classical *Spitzer* conductivity, with a modification at temperatures below 0.3 MK to better resolve the transition region with a minimal effect on the coronal part of the solution (Lionello et al. 2009; Mikić et al. 2013).

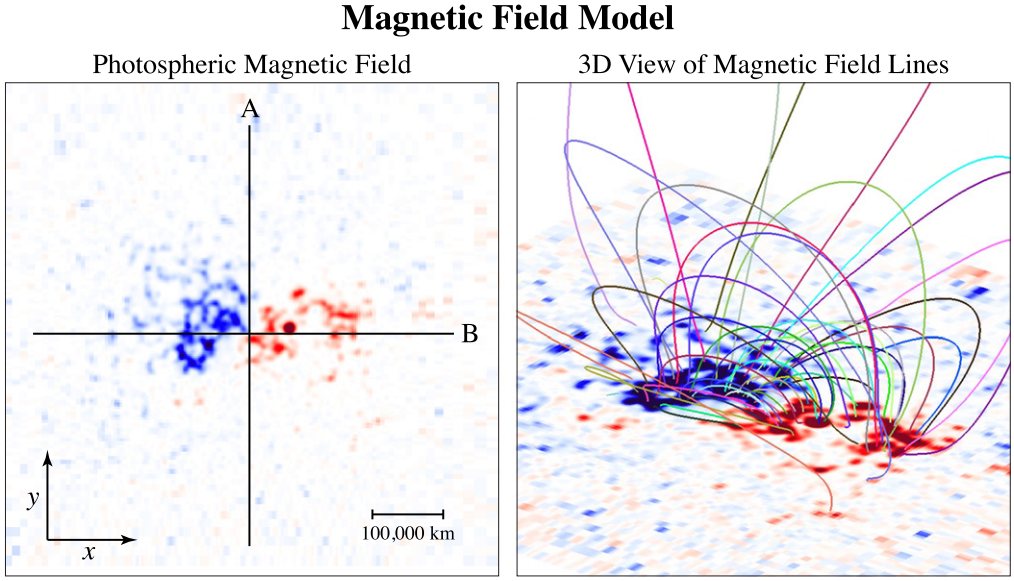

Figure 1. The left panel shows the photospheric magnetic field, interpolated onto our simulation mesh, and scaled between −750 G (blue) and 750 G (red), in the whole x–y simulation domain of dimension $1R_\odot \times 1R_\odot$. It was derived from a *SOHO*/MDI magnetogram of AR 7986 on 1996 August 30. The right panel shows a 3D view of selected magnetic field lines. Lines A and B are locations at which the temperature profiles are discussed in Section 4.

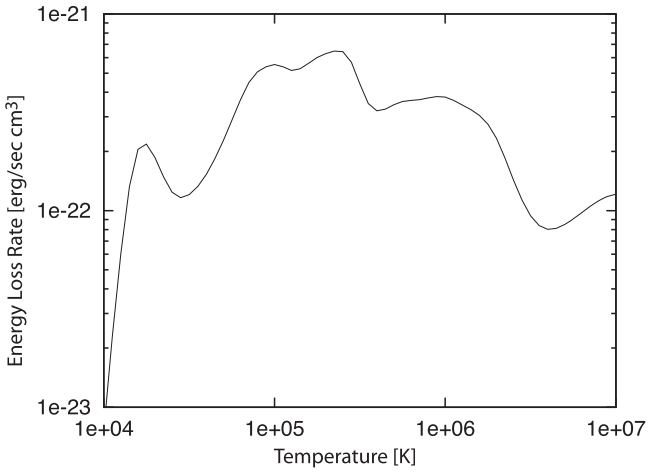

Figure 2. Radiative energy loss rate used in the computation. It is based on the CHIANTI (Dere et al. 1997) atomic database with coronal abundances.

The system of equations (Mok et al. 2005) is advanced in time to obtain the density and temperature profiles. The initial and boundary conditions have been described previously (Mok et al. 2008; Lionello et al. 2013). The solution, in general, does not settle into a state of steady equilibrium. The coronal solution in the AR core generally varies in time with oscillations of large amplitude. In some coronal locations temperature oscillates between transition-region values and coronal values. The time evolution is approximately periodic, but not sinusoidal, with variation on a timescale from 30 minutes to several hours. The solution appears to reach an approximate steady state only in some locations, such as the low corona and the quiet Sun away from the AR core. In the thermal nonequilibrium regions, the amplitude and period vary from location to location. The properties of thermal non-equilibrium are discussed in more detail in Section 3.2. We ran the simulation for approximately 27 hr and observed that the entire system evolved for several complete cycles. Our previous studies (Mok et al. 2005) showed that the system can reach an equilibrium when the heating rate is reduced, but the X-ray emission in these steady solutions is much smaller than observed by *Yohkoh*/SXT, and the temperature is much cooler than generally observed in active regions. We found that when the heating is selected to match observed X-ray emission, thermal nonequilibrium inevitably sets in (Mikić et al. 2013).

3. COMPARING SIMULATED EMISSION WITH OBSERVATIONS

To visualize the results, we compute the emissivity of the entire structure from the temperature and density solutions, followed by line of sight integration from an observer's viewing angle to obtain simulated emission images. For purposes of illustration, we compare emission in the three *SOHO*/EIT coronal EUV filters (171, 195, and 284 Å), and the *Yohkoh*/SXT soft X-ray Al–Mg filter, with specific observations. The emission is computed using the CHIANTI atomic database with coronal abundances. However, for purposes of comparison, we also compute emission using photospheric abundances (see the discussion below). During the 27 hr of simulation, typical features that are observed in active regions, including closed loops and fan loops, appear naturally in the simulated emission. Figure 3 shows the simulated emission images in the EIT 171 and 195 Å filters, observed directly from above at $t = 25.95$ hr. The simulated emission resembles the observed emission qualitatively, capturing some of the essential features in active region. For example, the region surrounding the neutral line is relatively dark, in agreement with observations. The closed loops and the fan loops are clearly visible. However, the connectivity of the loops does not fully agree with the observations, largely due to our imperfect magnetic field model. Figure 4 shows the emission in the EIT 171 Å filter at $t = 25.95$ hr when the AR is viewed from various perspectives. Two movies showing the appearance in the 171 and 195 Å filters as the active region is rotated with respect to the observer are available (see animations associated with figure 4). Multiple loops, including low-lying loops, high loops, and fan loops, are visible when viewed from various

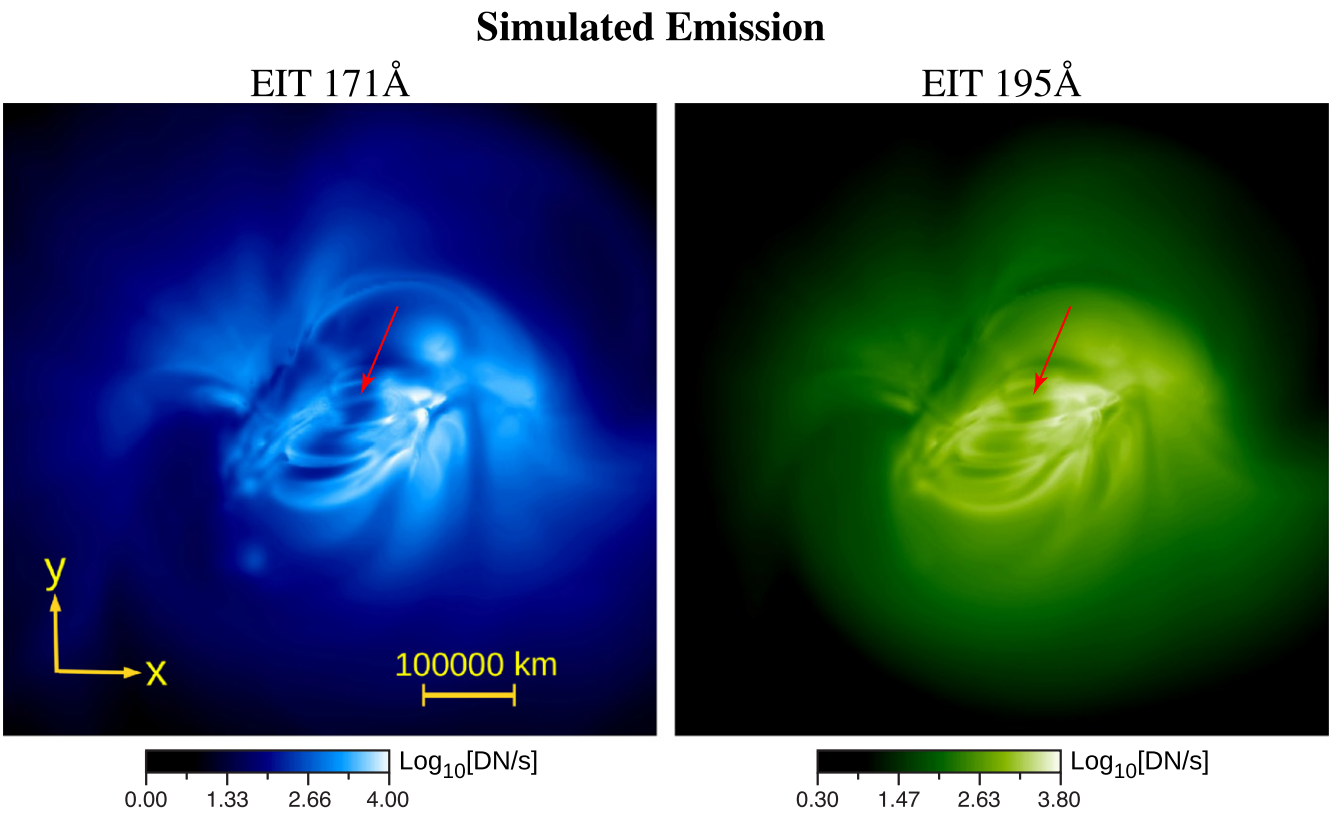

Figure 3. Simulated emission using coronal abundances computed at $t = 25.95$ hr in the EIT 171 and 195 Å filters, showing both closed loops and fan loops. The red arrow shows the loop whose neighborhood is analyzed in detail in the Appendix.

perspectives. Moss-like emission near the footpoints of the loops can also be seen. It is evident that thin coronal loops with nearly uniform cross-sections are present. The details of their 3D characteristics and why they form in particular locations will be discussed in a future paper. Importantly, these thin loops appear and fade naturally at specific locations for a heating model in which the entire corona is heated with one specification throughout the simulation. Quantitatively, the outer area away from the AR in Figure 3 appears to have too little emission compared to observations. This is due to the fact that our heating model is only applicable to strong-field regions, and we did not include a heating component that is applicable to the quiet Sun (Lionello et al. 2009). This aspect of the simulation could be improved in the future.

The following is a more detailed quantitative comparison between simulated and observed emission. For reference, Figure 5 shows the emission observed over the whole Sun in the four filters when the AR is near the center of the disk. In Figure 6, we compare simulated and observed emission in the active region. We first address the emission computed using coronal abundances (middle row). There are a few features common to the observed and computed images. For instance, the neutral line is relatively dim in 171 and 195 Å, while the high emission comes mostly from the areas with strong magnetic field. The emission in 284 Å and soft X-rays comes mostly from the apexes of the loops above the neutral line. The brightness along the fan loops in 171 Å compares well with observations. As shown in Figure 7, we find that the simulated and observed emission in the fan loops in the two regions selected is in the range 100–400 DN s^{-1}. There is a favorable comparison between simulated and observed emission in the coronal parts of high loops also. In the case of 195 Å, the fan loops and some high-altitude loops have emission in the range 60–200 DN s^{-1} and 200–320 DN s^{-1}, respectively, consistent with observations. For 284 Å, both the fan loops and the high loops have 3–10 DN s^{-1} in the computed and observed images. Although the simulated soft X-ray images do not show individual loops clearly, the overall brightness is approximately the same as observed.

It is evident that in all the EUV filters, but especially in 171 Å, and to a lesser extent in 195 Å, there is excessive emission in the model coming from the footpoints of closed loops in the strong-field regions. This problem is also present in other models (Schrijver et al. 2004; Brooks & Warren 2006; Warren & Winebarger 2006). For comparison, in the third row of Figure 6 we show the simulated emission computed using photospheric abundances. The core intensity is now comparable with observations, including the lower parts of the loops. This suggests that elemental abundances have a significant influence on the modeling of EUV emissions. The subject of elemental abundances and their spatial variation is very complex (e.g., Schmelz et al. 2012) and is beyond the scope of this paper. We do not suggest that this resolves the problem of excessive EUV emission in models; we merely show the emission computed for the two limiting cases (coronal versus photospheric abundances). A discussion of the effect of opacity on EUV emission is discussed below.

In order to confirm the location of the excess emission, we consider a "side view" through the active region. Figure 8 shows the emission observed over the whole Sun when the AR first appeared seven days earlier on August 23 at the east limb. In Figure 9 we compare the observed and computed emission

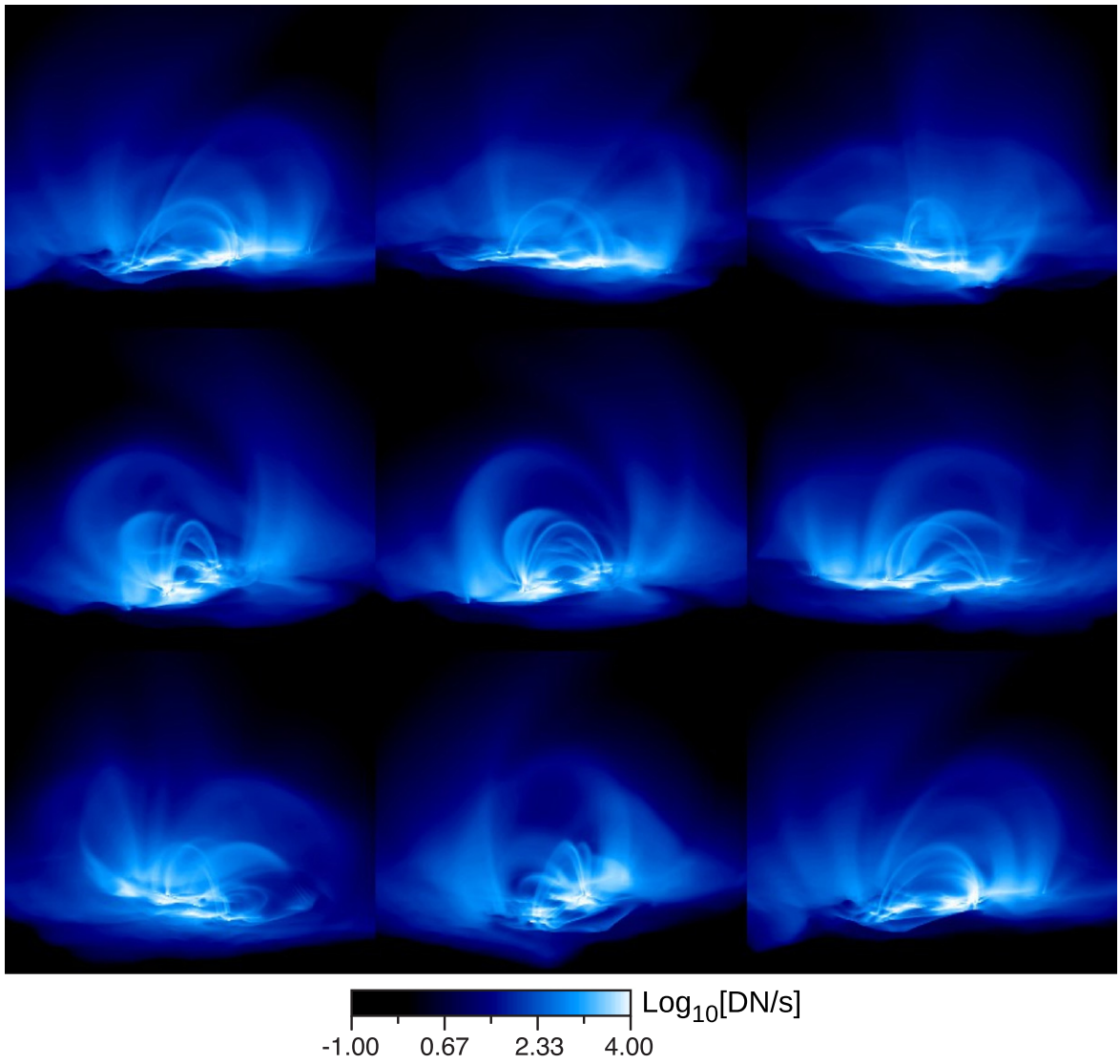

Figure 4. Simulated EIT 1717 Å emission of the entire active region at $t = 25.95$ hr when viewed from different perspectives. Starting from left to right, and top to bottom, successive views are approximately 40° apart. Movies of the emission when viewed by an observer that rotates with respect to the AR are available.
(Animations (a and b) of this figure are available.)

in the active region when it is on the limb. The middle row shows simulated emission using coronal abundances. The emission in the *coronal* part of the high loops (for $r \gtrsim 1.1R_{\odot}$) in the simulated images is roughly consistent with observations. For instance, both of them are in the range 200–500 DN s^{-1} in 171 Å. The details of the loop structures are different because the loops in the model do not match the observed ones, due to imperfections in the reconstruction of the coronal magnetic field (as discussed in Section 2). For instance, loops may reach different heights. Again, the lower part of the loops is overly bright in all EUV lines, but especially in 171 Å. For comparison, the third row shows simulated emission using photospheric abundances. Together with the top-view analysis, this confirms that the model using coronal abundances produces excessive emission in the lower corona and below. When computing simulated emission in Figures 6, 9, 10, and 11 we have mapped the temperature and density from our simulation in a box in Cartesian coordinates to a spherical sector in spherical coordinates before computing the emission, to properly treat the curvature effects that occur near the solar limb.

3.1. Effect of Atmospheric Opacity

Atmospheric opacity can contribute to the discrepancy by preventing emitted radiation from reaching the observer. The most common source of opacity comes from continuum absorption by cold material (typically prominences) containing H I, He I, and He II (Heinzel et al. 2008; Gilbert et al. 2011; Landi & Reale 2013). For example, absorption by prominence material is clearly visible in the top row of Figure 9 as a dark patch in the upper AR that extends above the limb in EIT 171, 195, and 284 Å. Although quiescent prominence material is not present in our simulation (nor is it the focus of our study), such

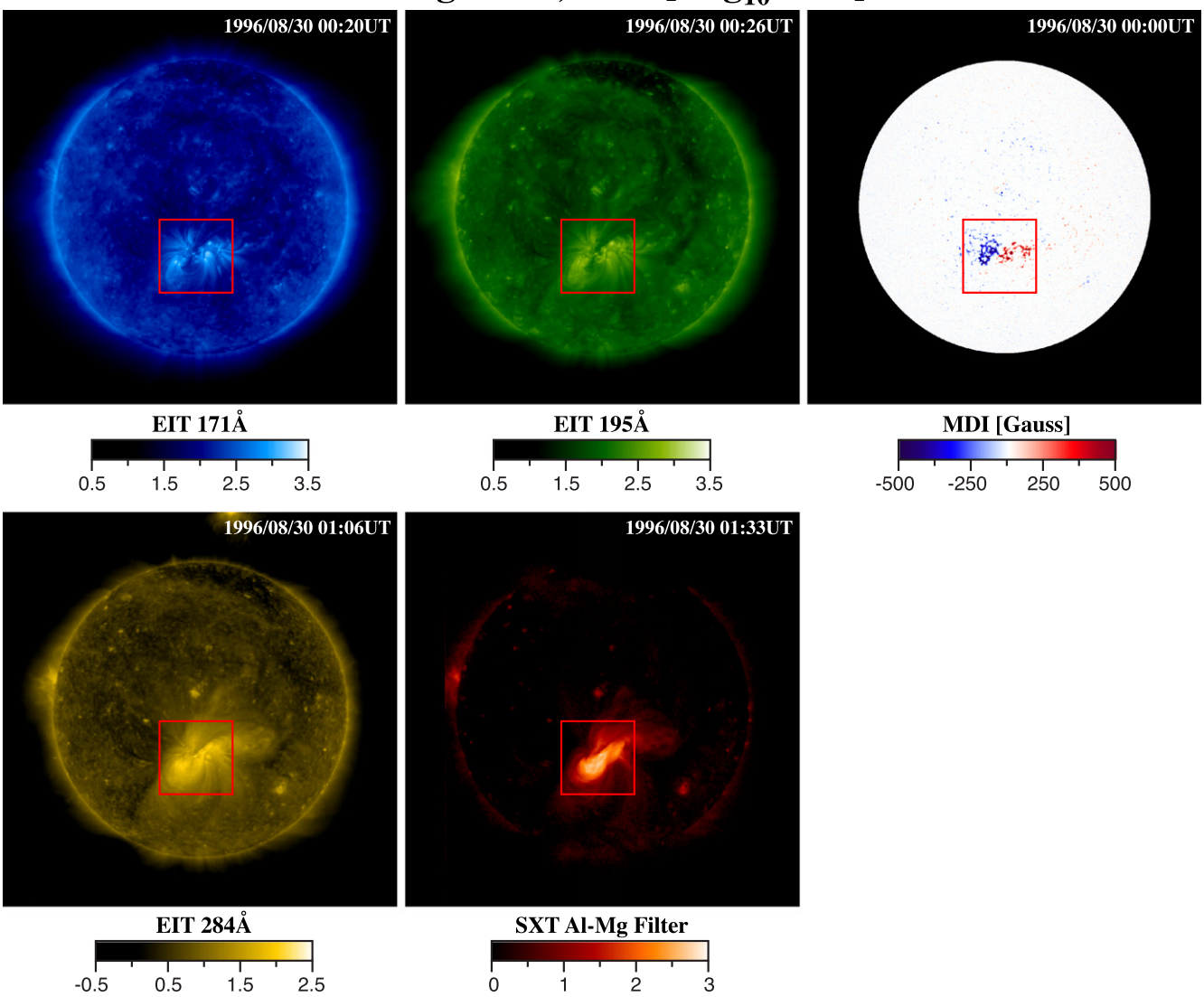

Figure 5. The whole Sun as it appeared in EUV and X-ray filters when the AR was at the center of the disk on 1996 August 30. The MDI magnetogram is also shown for reference. The red box is the area in which simulated emission is compared with observations in Figures 6 and 11.

absorption is important for lines of sight just off the limb, where cold material in the transition region and chromosphere will block out coronal emission produced on the far side of the plane of the sky that might otherwise be visible due to curvature. To account for this in our calculations, we use the wavelength-dependent cross-section formulas from Anzer & Heinzel (2005) and temperature-dependent populations of H I, He I, and He from the CHIANTI database (Landi et al. 2013) to calculate the optical depth τ_i. The wavelength dependent local extinction factor, $e^{-\tau_i}$, is then applied to the optically thin emissivity contribution of the given EUV channel at each point along the line of sight integral. Continuum absorption becomes relevant when the simulated AR is viewed near the limb, as shown in Figure 10. When it is included, some of the near-limb emission from behind the plane of sky is attenuated, causing the apparent position of the limb to move outwards; the effect is similar in the 195 and 284 Å channels (not shown). For the disk view, the effect of continuum absorption is negligible, primarily because the EUV emission forms above the chromospheric/transition region layer, so that the reduction in the simulated 171 Å footpoint/core intensity comes from resonant scattering. This might not always be the case if there is a significant filling factor of cool condensations forming within the coronal loops (e.g., Antolin & Rouppe van der Voort 2012 and Antolin et al. 2015). If statistically numerous enough, such condensations will serve to attenuate any EUV emission forming below. However, due to the geometric and thermal complexity of this phenomenon, we did not attempt to quantitatively account for it in this work.

Another consideration worth mentioning is the fact that some of the strongest coronal lines may be subject to significant resonant scattering due to optical depths under certain conditions (Schrijver et al. 1994). This will be the case for the Fe IX 171 Å line when enough Fe IX absorbers are present along the line of sight, such as the bright footpoint regions of coronal loops. Unfortunately, properly solving the transfer

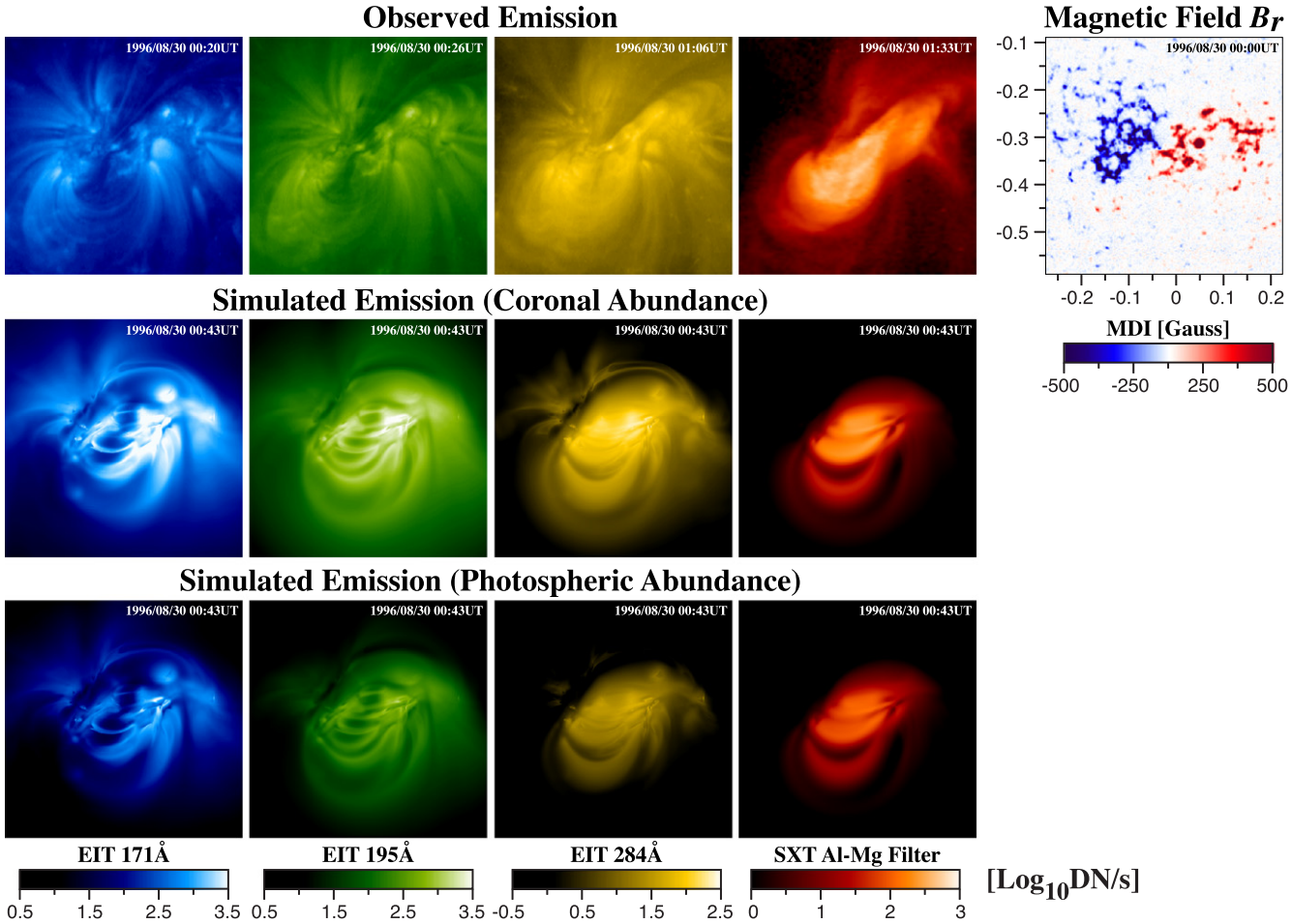

Figure 6. A quantitative comparison between observed emission on 1996 August 30, and simulated emission at $t = 25.95$ hr. The region of comparison is the red box shown in Figure 5. For reference, the MDI magnetogram in this region is also included, with distance units in solar radii. The emission is computed using the CHIANTI database with coronal abundances (middle row) and photospheric abundances (bottom row).

equation for resonant scattering involves numerous physical and geometrical considerations (e.g., Fischbacher et al. 2002), and requires either a limiting assumption about the symmetry of the system or sophisticated 3D ray-tracing and Monte Carlo methods (e.g., Wood & Raymond 2000), which are beyond the scope of this paper. Instead, a heuristic model is used to take into account this effect on the simulated EIT 171 Å emission where the resonant scattering opacities ought to happen, i.e., the over-bright footpoints of the loops. This is accomplished by using a uniformly reduced absorption cross-section in the formula for continuous absorption mentioned above, in such a way that the emissions are affected minimally in optically thin locations. The overall effect can be seen clearly as a relative reduction of emission at the brightest regions in the on-disk 171 Å image (Figure 11) and in the AR core just off of the limb (Figure 10). Applying the same technique to the dominant ions that contribute to the EIT 195 and 284 Å bandpass images (Fe XII and Fe XV) has little perceptible effect, as expected. Although a more elaborate treatment of opacity is required for quantitative comparison with observations, our heuristic model shows that this effect is not negligible and might help explain (a part of) the overly bright footpoint emission in this model.

3.2. Coronal Rain

As mentioned earlier, the solar atmosphere in our simulation is not in a state of thermal equilibrium, as evidenced by the time dependence of the emission. The EUV emission is highly inhomogeneous in space and shows the spontaneous episodic formation of thin coronal loops. This can best be visualized from a movie of the entire evolution of the emission in the 171 Å filter, which is available (see animation associated with figure 12). It can be seen that thin loops brighten and fade repeatedly in multiple locations. These changes in emission result from significant time variation of the plasma temperature and density in the corona, discussed in more detail in the next section. In fact, most of the corona within the AR core undergoes evaporation–condensation cycles. The Appendix quantifies the extent of this variation for an interesting loop bundle.

Here we focus on a typical event in which a condensation can be seen to fall down one of the legs of a spontaneously formed coronal loop. This "blob" is followed in detail in Figure 12, which shows a condensation in one of the loops, as seen in simulated 171 Å emission, which is tracked by an arrow in the figure. The condensation first appears half way down

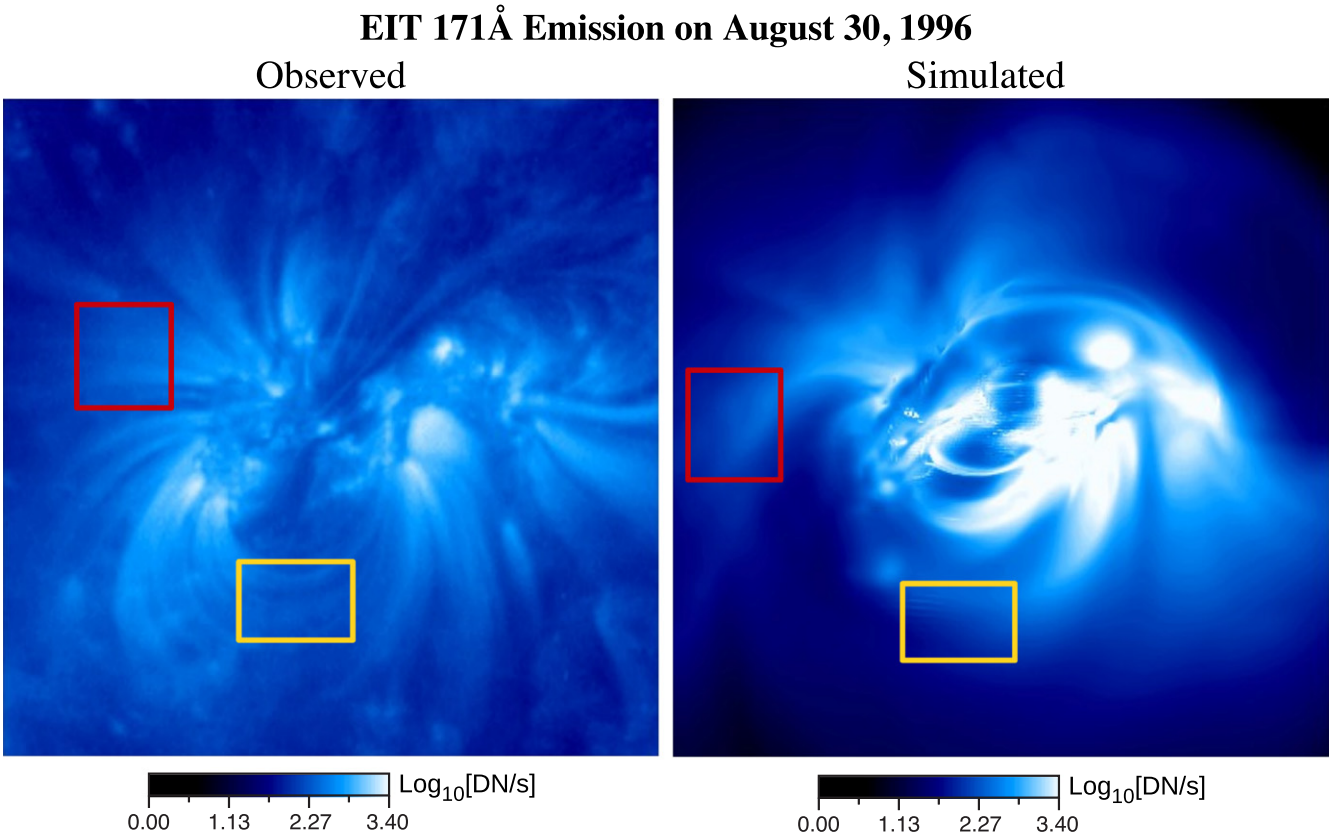

Figure 7. A comparison of the observed and simulated 171 Å emission in the *coronal* part of loops at $t = 25.95$ hr. The red boxes show regions with fan loops of comparable intensity; the yellow boxes show regions with high loops of comparable intensity. The areas selected for comparison are not identical because the topology of the simulated loops is different from the observed loops due to imperfections in the magnetic model.

from the apex of the loop, and subsequently falls down the leg of the loop, eventually splashing into the chromosphere. This blob resembles observations of coronal rain (e.g., De Groof et al. 2004, 2005). Antolin & Rouppe van der Voort (2012) and Antolin et al. (2015) noted that observed coronal rain actually consists of showers composed of many smaller blobs with a large variation in temperature, from transition-region to chromospheric values. It is likely that our spatial resolution may not be sufficient to resolve these smaller features. The blob falls at approximately 42 km s^{-1} toward the footpoint. Similar plasma condensations can be seen in multiple locations throughout the entire simulation. Such condensations have also been seen in other simulations (Müller et al. 2004, 2005; Mendoza-Briceño et al. 2005; Antolin et al. 2010; Xia et al. 2011; Luna et al. 2012; Fang et al. 2013).

4. THERMAL STRUCTURE PRODUCING THE EMISSION

Loops are conspicuous features in active-region emission. We have previously investigated the relationship between the formation of loops and the evolution of the coronal temperature and density (Mok et al. 2008). Here we investigate in detail the relationship between the emission and the thermal structure. Figure 13 shows the highly inhomogeneous temperature profiles in two vertical planes at $t = 12.85$ hr. Panel (a), in the y–z plane, is a slice roughly aligned with the neutral line (designated by line A in Figure 1). The local field lines are thus predominantly perpendicular to this plane. Panel (b), in the x–z plane, is roughly perpendicular to the neutral line (designated by line B in Figure 1). The local field lines are mostly parallel to this plane. A temperature depression can be seen as a blue dot in (a), and as a loop-like structure in (b). This feature is aligned along a coronal loop that can be seen in the 171 Å emission. Figure 14 shows a time sequence of the temperature in the region denoted by a black box in Figure 13 in the y–z plane. A movie of the evolution of the temperature in this same region covering approximately 21 hr is available (see animation associated with figure 14). After an initial transient, two local temperature depressions begin to appear at $t = 12.85$ hr. These two cool spots are tracked by arrows as features "A" and "B" in Figure 14. Spot A, which does not have circular shape, reaches a minimum temperature of 0.24 MK. Spot B reaches a minimum temperature of 1.9 MK.

A coronal loop that is roughly parallel to the x axis (i.e., perpendicular to the y–z plane) appears in the 171 and 195 Å emission at spot A during the time interval covered by Figure 14. When visualized in 3D, the temperature depression in the y–z plane is in fact the cross-sectional area of a loop-like structure. The "loop" itself is a thin, relatively low-temperature tunnel embedded in a high-temperature region with its axis following a magnetic field line. Figure 15 shows the 1.8 MK temperature isosurfaces at $t = 25.95$ hr, indicating that the temperature tunnel follows a magnetic field line. The temperature is less than 1.8 MK inside the surface and more than 1.8 MK outside the surface. The magnetic field line that passes through spot A is seen to thread the inside of the temperature tunnel. This cool temperature tunnel, together with an enhanced density, is a condensation in the corona, and emits the EUV radiation that is seen as a coronal loop in emission.

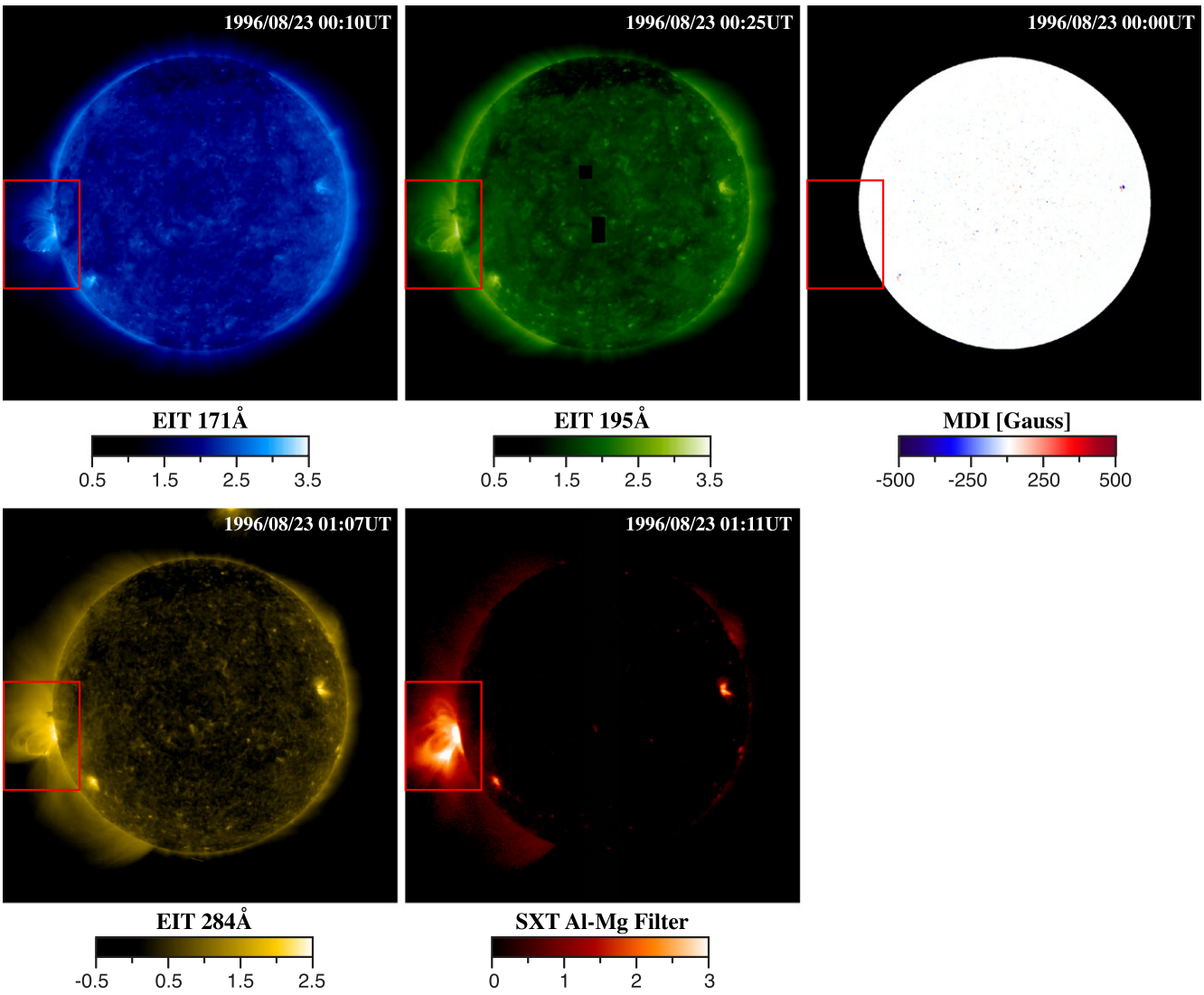

Figure 8. The whole Sun as it appeared in EUV and X-ray filters when the AR was at the limb on 1996 August 23. The red box is the area in which simulated emission is compared with observations in Figures 9 and 10.

During the 27 hr of simulation, multiple highly localized temperature tunnels appear and subsequently fade, similar to the sequence shown in Figure 14. Their lifetimes range from 30 minutes to several hours, as shown in the movie, which is typical of the lifetime of coronal loops. Such long-period cycles have been observed by Auchère et al. (2014) in *SOHO*/EIT observations, and by Froment et al. (2015) in *SDO*/AIA observations. The properties of such loops have been studied in detail in Papers I, II, and III.

The finite radius of the temperature tunnel is an indication that the individual field lines in a small flux tube have similar temporal characteristics; therefore, they evolve in a synchronized manner. However, they do not maintain their coherence forever because of the slight difference in the period of their thermal nonequilibrium cycles. Eventually, the temperatures of adjacent field lines drift out of phase, causing the temperature tunnel to disintegrate. The coherence time therefore becomes the lifetime of the loop. This behavior has been observed statistically, as shown by Antolin & Rouppe van der Voort (2012). Neighboring field lines are generally observed to display coronal rain at similar times. They suggest that there is a characteristic coherence in the transverse direction for the heating. The Appendix presents an analysis of the properties of a bundle of field lines, and discusses the coherence of neighboring field lines. A detailed study of why a tunnel forms around a particular field line will be addressed in a future paper.

5. DISCUSSION AND CONCLUSIONS

We have presented a model to compute the thermal structure of the corona in active regions, and have applied it to AR 7986, which was observed in 1996 August. The model incorporates the important physical effects that affect energy transport in the corona, including heating, radiative energy loss, and thermal conduction. The heating model is inspired by a turbulent

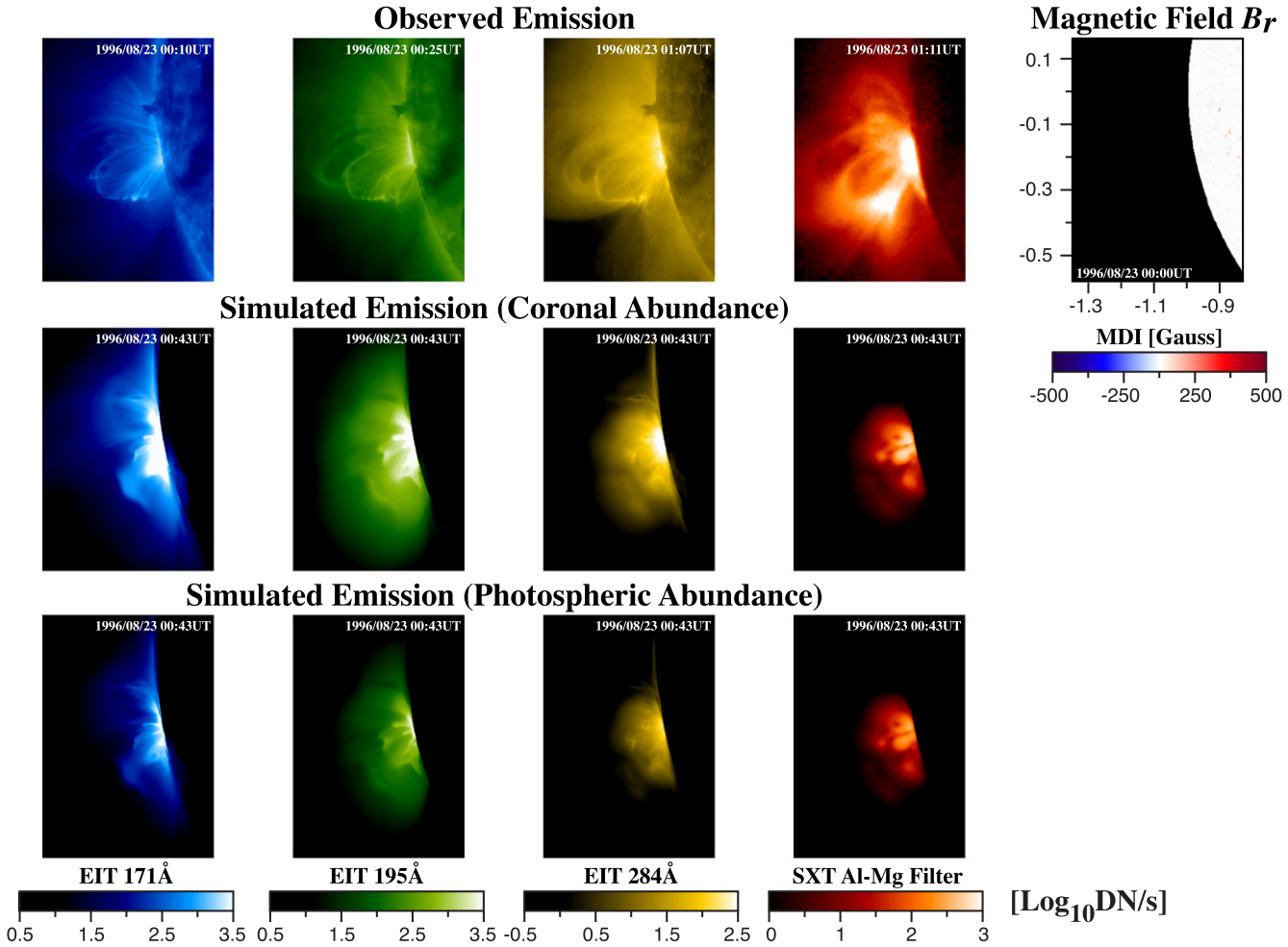

Figure 9. A quantitative comparison between observed emission on 1996 August 23, and simulated emission at $t = 25.95$ hr. The region of comparison is the red box shown in Figure 8. For reference, the MDI magnetogram in this region is shown to locate the solar limb, with distance units in solar radii. The emission is computed using the CHIANTI database with coronal abundances (middle row) and photospheric abundances (bottom row). It is apparent that excessive emission comes from the lower atmosphere. The simulated emission in the coronal part of the loops is consistent with observations.

Alfvén wave dissipation theory (Rappazzo et al. 2007, 2008). One of the fundamental properties of this model is that plasma heating occurs mostly at low altitudes in the corona (so-called footpoint heating) because of its strong dependence on the magnitude of the local magnetic field. We find that the simulated EUV emission from our simulation spontaneously produces thin loop-like structures that resemble coronal loops. These loops appear and fade in many locations, producing a very dynamic corona with significant small-scale inhomogeneities in the emission. We have traced these structures to the phenomenon of thermal nonequilibrium, in which plasma is observed to cycle through condensation–evaporation cycles with large amplitude oscillations. In the active region that we simulated, some coronal locations are in a persistent state of thermal nonequilibrium, whereas others are in a quasi-steady state. We have quantified the extent of this effect for a interesting bundle of field lines. In general, the loops that experience thermal nonequilibrium tend to have field lines whose footpoints anchor in strong-field regions, while the steady regions tend to have either low-lying loops or high loops anchored at the edge of the AR. The "footpoint heating" aspect of this model is not unique. There exist other similar models with similar solutions (e.g., Müller et al. 2003).

A quantitative comparison of models with observations is an important validation of the underlying physics. We have carefully compared simulated emission from our model with observed emission in EUV and soft X-rays. We find that we can reproduce some of the characteristic features in an entire active region across a range of coronal temperatures. There is good quantitative agreement between our simulated emission and observed emission, though there are significant discrepancies as well. The lifetimes of individual loops in our simulation, as measured by the periods of the thermal nonequilibrium cycles, compare well with those deduced from observed loops (e.g., Auchère et al. 2014; Froment et al. 2015). In addition, the highly dynamic nature of the model produces plasma flows and condensations that resemble coronal rain (De Groof et al. 2004, 2005; Antolin & Rouppe van der Voort 2012; Antolin et al. 2015).

The most serious difficulty of the model is the excessive emission from the lower atmosphere when compared with observations. When the AR is viewed from above, the overall

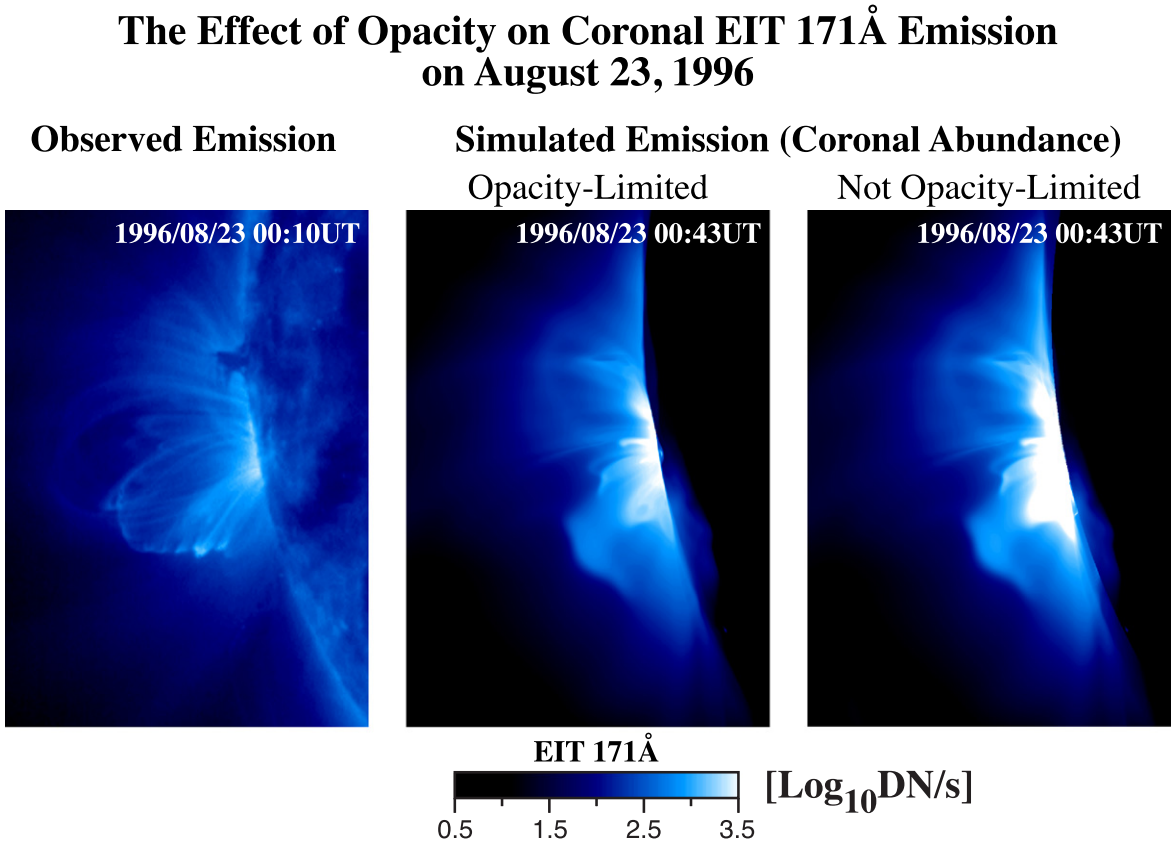

Figure 10. Comparison of the effect of opacity on 171 Å emission for a limb view of the active region. This is the same region as that shown in Figure 9. The middle image, which includes opacity, shows that the emission in the lower corona is reduced compared to the non-opacity-limited estimate, bringing it closer to the observed image, but the effect is not sufficient to explain the discrepancy.

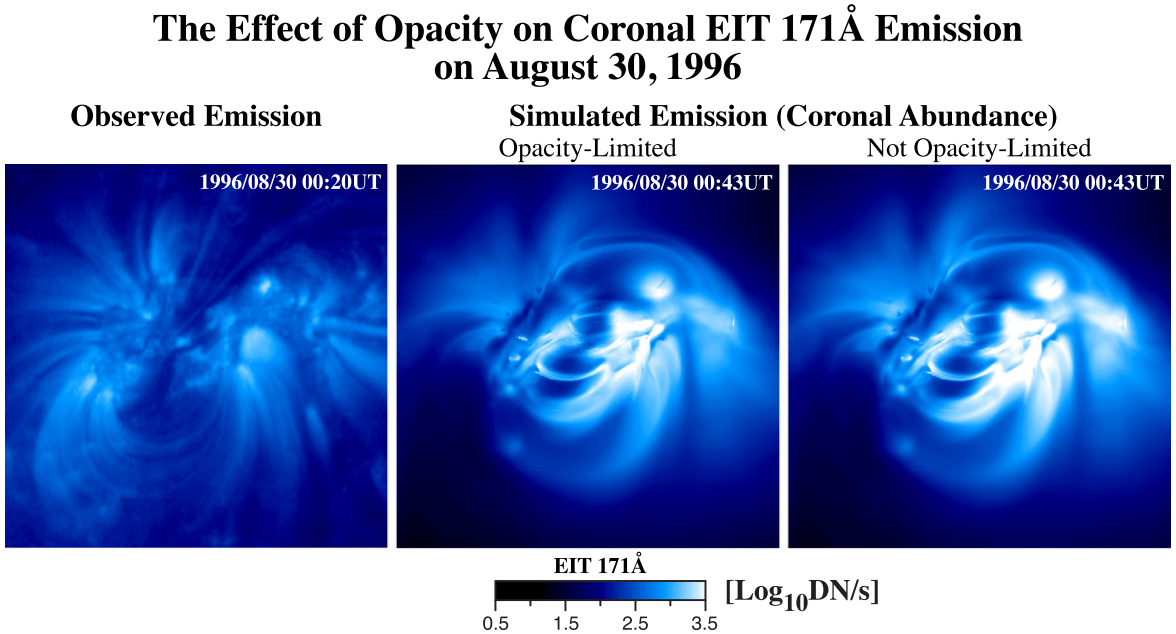

Figure 11. Comparison of the effect of opacity on 171 Å emission for a disk-center view of the active region. This is the same region as that shown in Figure 6. The effect of opacity reduces the emission, but this alone does not reduce the emission from the lower legs of the loops enough. The 195 and 284 Å images (not shown) are not appreciably altered with this model, because of the intrinsically lower line oscillator strengths and smaller column density of the Fe XII and Fe XV ions.

simulated emission in the core when using coronal abundances is approximately four times larger than that observed by EIT in the 171 Å filter. Interestingly, this difficulty also appears in many other models, even when different heating specifications are used (e.g., Schrijver et al. 2004; Brooks & Warren 2006; Warren & Winebarger 2006). We have examined the

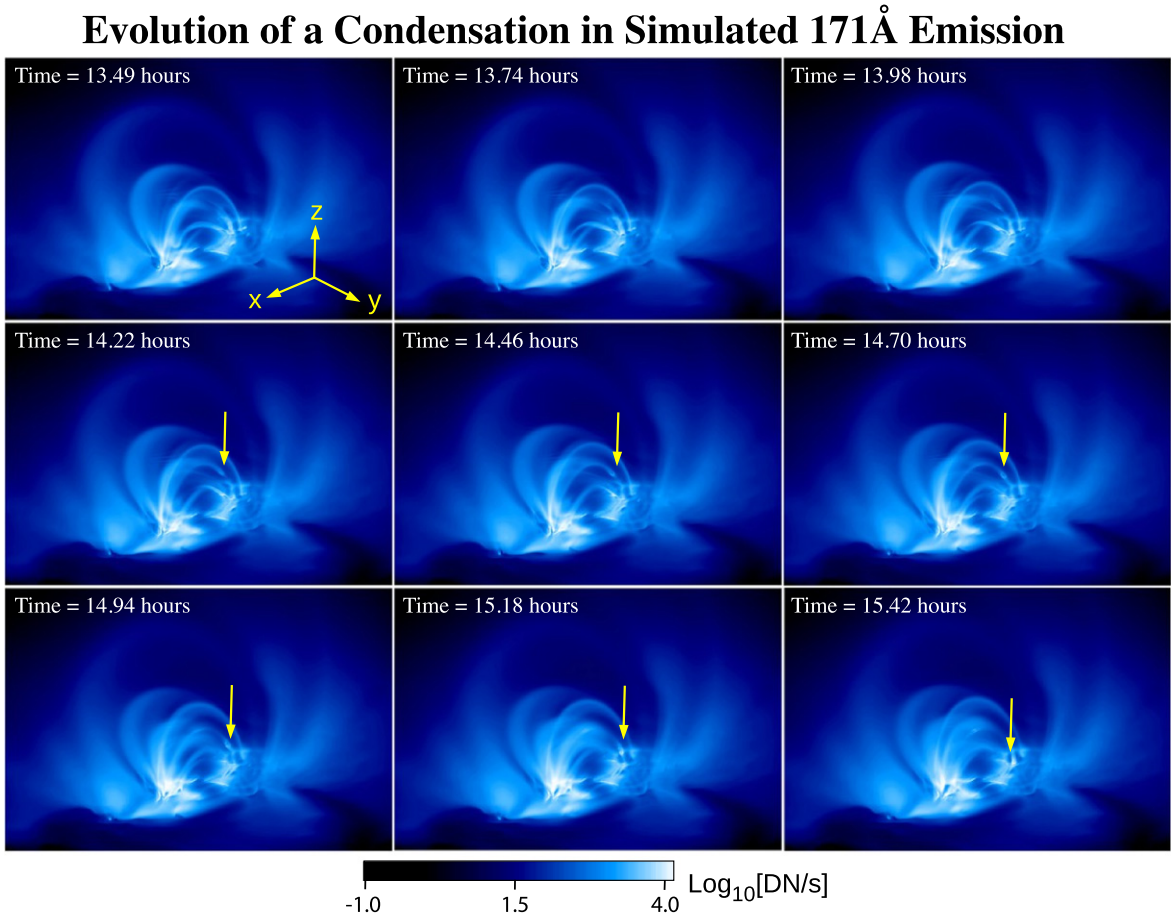

Figure 12. A time sequence of simulated emission in 171 Å, showing the dynamic nature of the AR emission. Multiple thin loops are visible. A blob of plasma, tracked by the arrows, can be seen to condense halfway down the leg of one of the loops, and subsequently falls to the chromosphere. Such features are likely manifestations of coronal rain.

(An animation of this figure is available.)

contribution of two possible sources of this discrepancy: elemental abundances and atmospheric opacity. We have shown that when the simulated images are computed using photospheric, instead of coronal, abundances, the emission from the previously over-bright regions is significantly reduced, and becomes comparable to what is observed. This suggests that element abundances may have a significant influence on coronal emission. A rigorous treatment would require a model that takes into account the spatial distribution of elemental abundances. This is prohibitive at the moment. Our results are merely suggestive, and await a more comprehensive treatment.

We also examined the effect of atmospheric opacity on coronal emission. We illustrated how continuum absorption may be relevant for attenuating EUV emission near the limb, and how the brightest 171 Å emission may be susceptible to resonant scattering, both when looking down on an active region (i.e., near disk center), and also when looking from the side (i.e., on the limb). In general, the effect is more pronounced when the AR is viewed at the limb. However, a more elaborate treatment is required if the full effect of opacity is to be included, and this is beyond the scope of the present paper.

Finally, we relate this work to our previous work (Mok et al. 2008). In general, we have found that the features seen in EUV emission in the present model appear to be much "sharper" than in the previous model, and significantly more loop-like structures appear in the present model. There are four major effects that might contribute to this difference: (1) the spatial resolution (number of grid points) in the calculation; (2) the heating profile (especially its tendency to be concentrated at loop footpoints); (3) the spatial structure of the magnetic field in the photosphere; and (4) the viscosity used in the simulation. It is to be noted that the numerical techniques that we use to solve the equations contribute to the true viscosity in the calculation. Namely, there is an explicit bulk viscosity that is specified as a parameter, and an additional numerical component that is proportional to the grid spacing (a so-called "upwind" viscosity). This numerical viscosity is reduced when higher spatial resolution is used in the calculation.

When we compare the present model with the previous one, we find that the heating profiles, even though they were different, both had sufficient concentration in the lower atmosphere to produce thermally unstable solutions. The magnetic field in the photosphere had very similar properties in the two models. Hence, we conclude that the difference in the results is due to spatial resolution and the effect of viscosity. The newer model had grid cells in the core of the active region that were four times smaller than the previous model. This allowed us to reduce both the bulk viscosity and

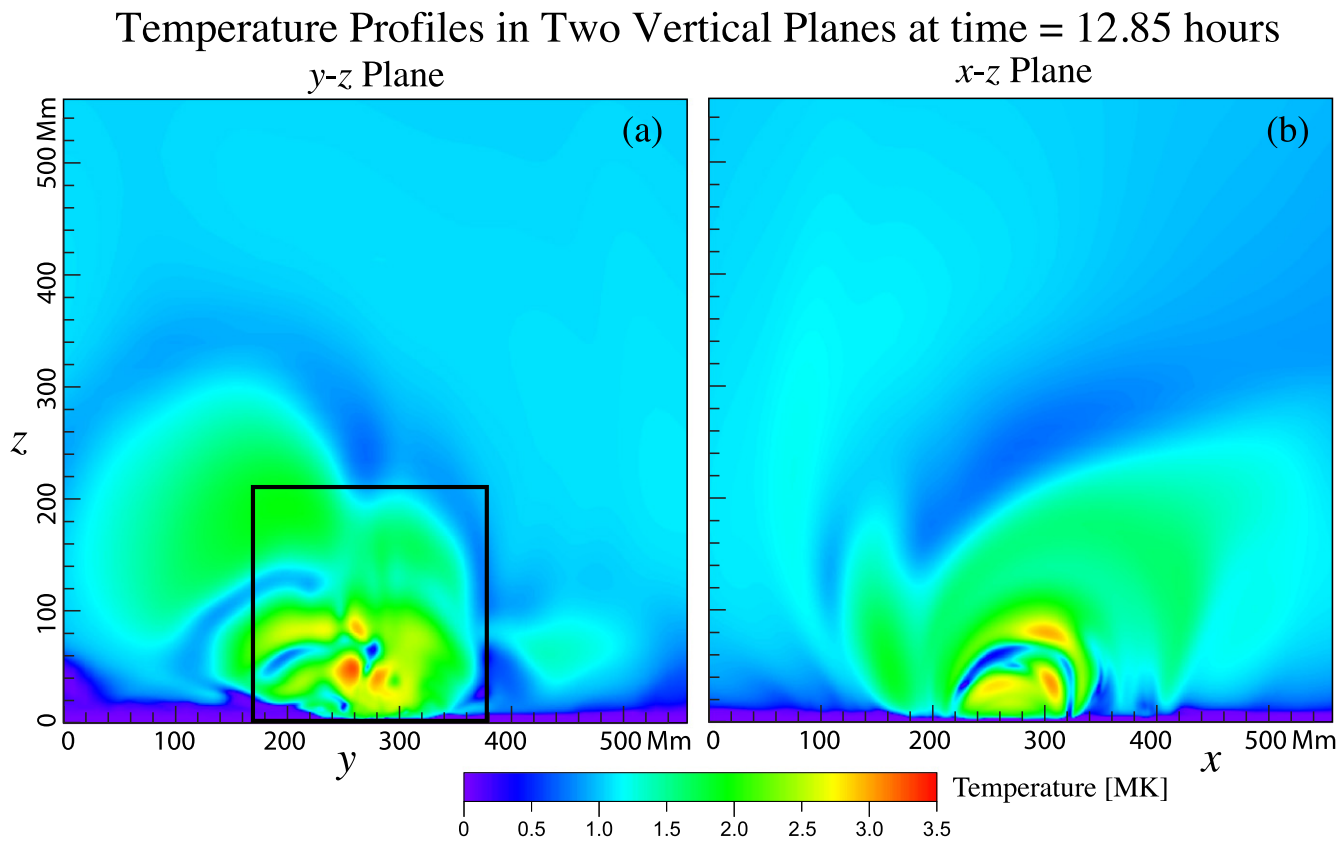

Figure 13. Temperature profiles in the y–z plane (a) and x–z plane (b) at an instant when a coronal loop is visible. The y–z slice is along line A in Figure 1, i.e., roughly along the neutral line. The x–z slice is along line B in Figure 1. The black box, of dimension $0.3R_\odot \times 0.3R_\odot$, indicates the region whose evolution is shown in the panels of Figure 14.

the numerical viscosity significantly in the newer model. The viscous dissipation time τ_ν, for a length scale L, is given by $\tau_\nu = L^2/\nu$, where ν is the viscosity. In the old model, we used a viscosity for which the viscous dissipation time for a length scale $L = R_\odot$ was 160 hr. In the present model, the viscous dissipation time was 24,000 hr. The numerical viscosity in the new model is estimated as being an order of magnitude higher than this bulk viscosity (i.e., with a corresponding $\tau_\nu \sim 2400$ hr), so that overall, the total viscosity in the new model is more than an order of magnitude lower than that in the previous model. Hence, we attribute the enhanced tendency of coronal loop formation in the new model to the effect of reduced viscosity. This implies that future models with even higher spatial resolution, which are practical even today with massively parallel supercomputers, may produce results that look even more like the corona. Of course, the inclusion of other physical effects, such as improved resolution in the photospheric magnetic field, and the evolution of the magnetic field in the photosphere and corona during the simulation, might enhance this effect even more.

This work was supported by NASA's Heliophysics Theory Program. Computational resources were provided by the NASA High-End Computing (HEC) Program through the NASA Advanced Supercomputing (NAS) Division at Ames Research Center. We thank Amy Winebarger for useful discussions. We also thank the anonymous referee for constructive suggestions.

APPENDIX
ANALYSIS OF A LOOP BUNDLE

In order to characterize the nature of thermal nonequilibrium occurring in our simulation, we chose a 15×15 grid of positions in the y–z plane, at a fixed value of x, centered at the location at which a coronal loop forms in the synthesized EUV 171 Å emission. This is a thin loop that is visible at $t = 25.95$ hr, and is indicated by a red arrow in Figure 3. We label these points by two indices, j and k, with j denoting the y position and k denoting the z position. The points were separated by 0.002 solar radii (1.4 Mm) in the y and z dimensions, so that the area covered by this square grid was 0.028×0.028 solar radii. We traced 225 loops that passed through the points on this grid for analysis. Figure 16 shows these field lines. The loops range in length from 104 to 169 Mm. The approximate coronal volume spanned by this bundle of loops is approximately 50,000 $(\mathrm{Mm})^3$.

We extracted the solutions from the 3D simulation along these field lines as a function of time and length along the loops. We also ran simulations using a 1D code (described by Mikić et al. 2013) along these 225 field lines individually, for the same parameters, to verify that the behavior observed in the 3D run was reproduced. By and large, the results between the 1D and 3D runs were very similar, except for the features described below. In particular, the observed propensity of the loops to experience thermal nonequilibrium was very similar. We therefore use this set of loops to quantify the extent of thermal nonequilibrium.

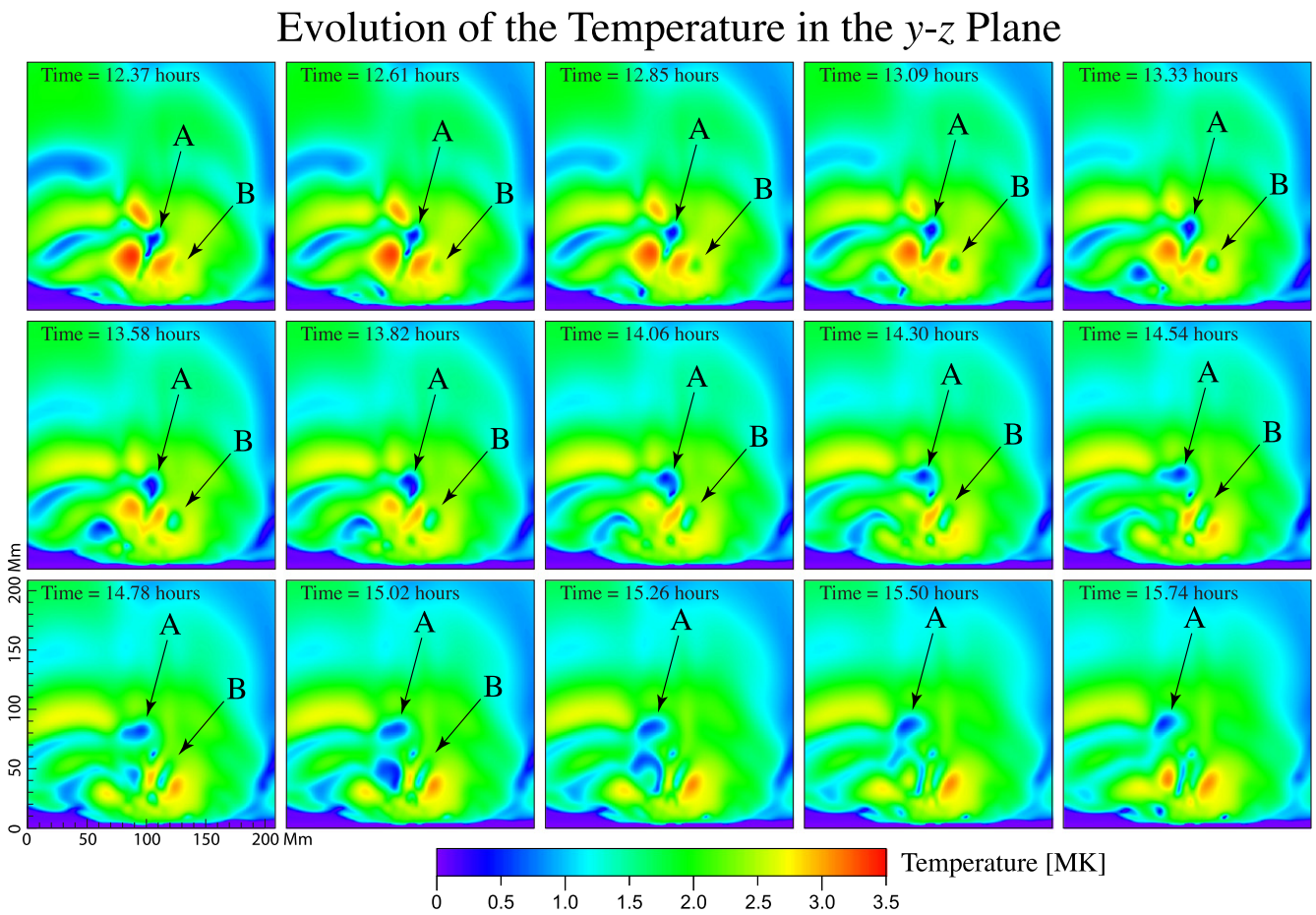

Figure 14. The evolution of the temperature in the y–z plane in the region of the black box in Figure 13(a). The features "A" and "B," which are followed in time by arrows, are the locations of condensations that appear as coronal loops in EUV emission. A movie of the evolution of the temperature in this same region covering approximately 21 hr is available.

(An animation of this figure is available.)

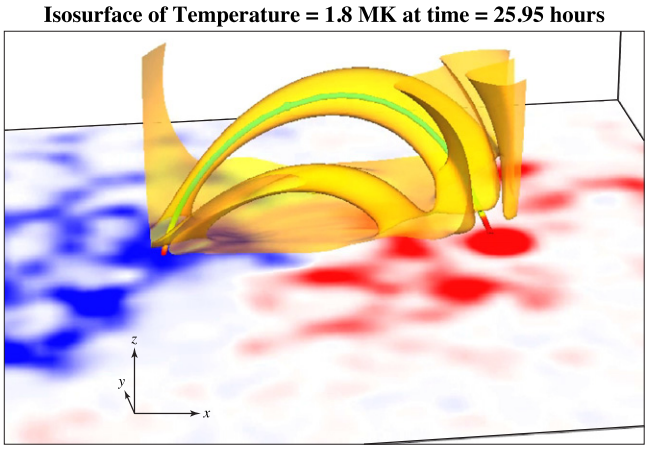

Figure 15. A temperature isosurface at 1.8 MK, showing temperature tunnels corresponding to EUV loops. The green line is the magnetic field line along the axis of one of the loops. It is also the central field line in the bundle of loops analyzed in the Appendix.

In this comparison we did notice that it was necessary to raise the viscosity in the 1D loop runs significantly to match the behavior seen in 3D. This is understandable since in 3D our (isotropic) viscosity operator acts in all directions, along the loops as well as across them. In particular, since thermal conductivity generally acts to strongly smooth gradients along field lines, the gradients across field lines are expected to dominate most of the time, and these gradients are obviously not included when we model loops individually in 1D. Hence the 3D loop behavior will in general tend to be more "diffusive." To some extent, the cross-field thermal conduction, which arises purely from numerical discretization errors in the implementation of parallel thermal conduction in 3D, may also have this diffusive effect. Hence it is not surprising that the 3D evolution is observed to be more diffusive. Of course, as the numerical resolution in the 3D calculation is increased, allowing for reduced viscosity and cross-field conduction, the results from the 3D code ought to approach those from the 1D simulations. Indeed, the 1D runs can give us a glimpse of what behavior can be expected from high-resolution 3D runs. These results will be discussed in more detail in a forthcoming publication.

Along this same line, we noticed that neighboring loops tend to be more correlated in their thermal nonequilibrium cycles in 3D than in the 1D solutions. In particular, when we reduced the viscosity in the 1D solutions we observed that the fraction of full condensations (i.e., with material condensing to

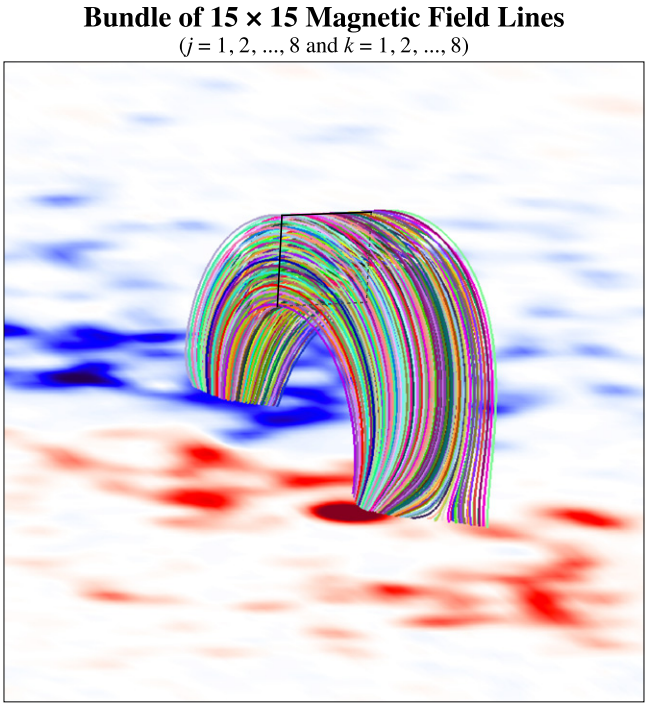

Figure 16. Traces of the magnetic field lines in the bundle whose properties are analyzed in the Appendix. The field lines are launched from points on a 15 × 15 grid inside the black square in the y–z plane.

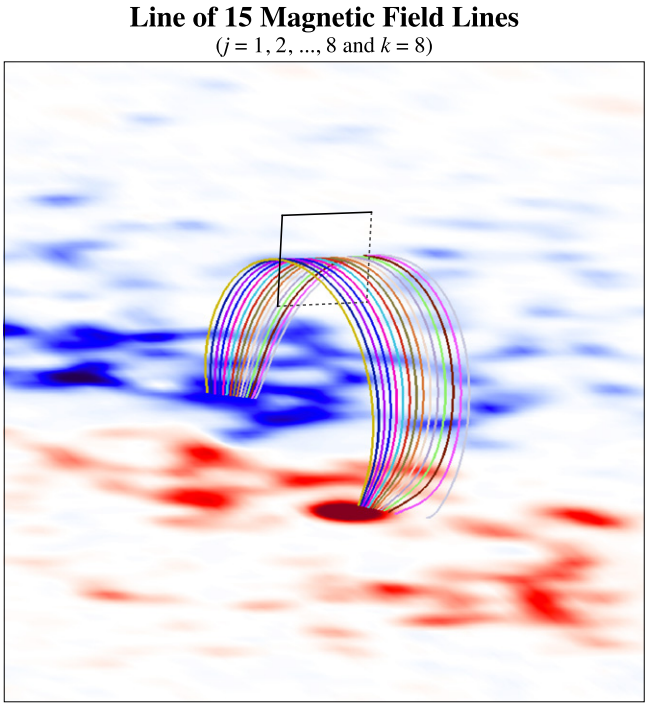

Figure 18. Traces of the magnetic field lines in the middle row of the 15 × 15 grid whose properties are analyzed in the Appendix. The temperature evolution shown in Figure 17 is along these field lines.

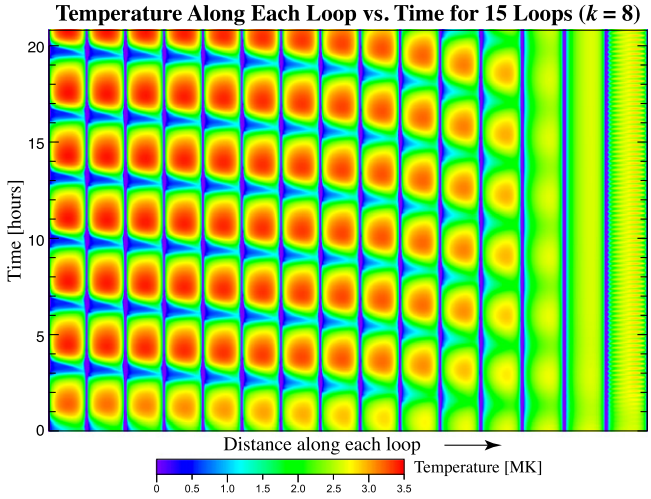

Figure 17. The evolution of the temperature for each of the 15 field lines along the middle row of the bundle (with $k = 8$). Each panel shows the temperature for an individual field line, with time running vertically, and distance along the loop length running horizontally. The 15 images are stacked side-to-side horizontally, with increasing values of j left-to-right.

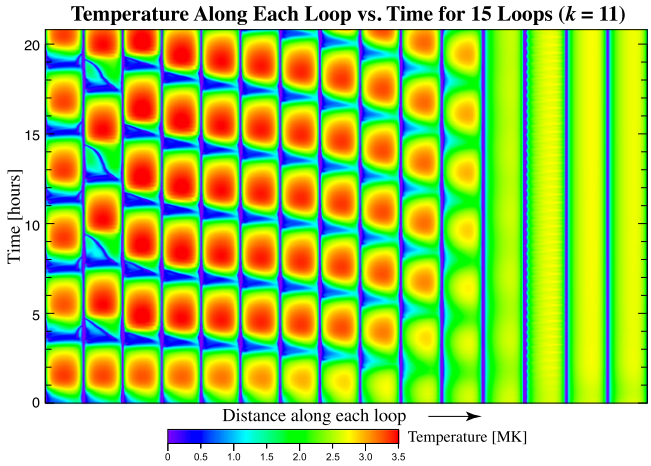

Figure 19. The evolution of the temperature for each of the 15 field lines along the eleventh row of the bundle (with $k = 11$). Each panel shows the temperature for an individual field line, with time running vertically, and distance along the loop length running horizontally. The 15 images are stacked side-to-side horizontally, with increasing values of j left-to-right.

chromospheric temperatures in the corona) increased. These condensations might be identified with "knots" of coronal rain in observations. It is thus likely that high-resolution simulations in 3D would be more dynamic and would have smaller-scale features, perhaps resembling observations more closely. On the other hand, it is important to keep in mind that certain physical effects, which can in principle be included in 3D simulations but not in 1D simulations, can also lead to correlation between neighboring loops. An example is the sympathetic cooling effect, in which transverse perturbations can trigger catastrophic cooling in neighboring loops (Fang et al. 2013). Another example is the thermal (entropy) mode, discussed by Antolin et al. (2015), which occurs in the presence of small (but finite) perpendicular thermal conduction. Caution is therefore required when interpreting the results from 1D simulations.

As an illustration, Figure 17 shows the evolution of the temperature along 15 field lines for a set of 1D runs with low viscosity. The footpoints of these field lines lie along the horizontal line with $j = 1, 2, \cdots, 15$ and $k = 8$. The corresponding field line traces are shown in Figure 18. Note that the first 13 field lines experience thermal nonequilibrium cycles, whereas the last 2 have stable solutions. (In fact, the last field

line has a solution with small-amplitude high-frequency oscillations, with a period of ≈15 minutes, but we label this as "stable" for the present purposes.) The period of the thermal nonequilibrium cycle for the first 13 field lines ranges from 3.08 to 3.30 hr. Figure 19 shows the temperature for the 15 field lines with footpoints on the horizontal line with $j = 1, 2, \cdots, 15$ and $k = 11$. Note that the first 11 undergo thermal nonequilibrium cycles, and the last 4 are stable. Also, in the first three field lines, full condensations to chromospheric temperatures that fall down the loops legs are visible.

We now consider the gross statistics for these loops. Of the 225 loops, 140 experienced thermal nonequilibrium, ranging in period from 3.0 to 4.8 hr, and 85 were stable. About 16 experienced significant deep condensations; the rest (124) experienced incomplete condensations.

These simulations also give us an estimate of the decorrelation length scale across loops. Recalling that each loop is displaced by 1.4 Mm from its neighbors in the starting y–z plane, we see that the decorrelation scale can be as short as 1.4 Mm (i.e., the second and third loops in Figure 19 show that the second one has a significant full condensation, whereas the third one has a smaller condensation). However, for the large-scale thermal nonequilibrium cycles, it seems that, at least for this bundle of loops, the decorrelation length is more like 5–10 Mm, over which the period of thermal nonequilibrium can change substantially. In time, neighboring loops will exhibit significantly different properties because their (quasi-) periodic evolution will become out of phase.

REFERENCES

Ahn, K., Chae, J., Cho, K., et al. 2014, SoPh, 289, 4117
Antiochos, S. K., & Klimchuk, J. A. 1991, ApJ, 378, 372
Antiochos, S. K., MacNeice, P. J., & Spicer, D. S. 2000, ApJ, 536, 494
Antiochos, S. K., MacNeice, P. J., Spicer, D. S., & Klimchuk, J. A. 1999, ApJ, 512, 985
Antolin, P., & Rouppe van der Voort, L. 2012, ApJ, 745, 152
Antolin, P., Shibata, K., & Vissers, G. 2010, ApJ, 716, 154
Antolin, P., Vissers, G., Pereia, T. M. D., Rouppe van der Voort, L., & Scullion, E. 2015, ApJ, 806, 81
Anzer, U., & Heinzel, P. 2005, ApJ, 622, 714
Aschwanden, M. J., Alexander, D., Hurlburt, N., et al. 2000, ApJ, 531, 1129
Aschwanden, M. J., Newmark, J. S., Delaboudiniere, J. P., et al. 1999, ApJ, 515, 842
Auchère, F., Bocchialini, K., Solomon, J., & Tison, E. 2014, A&A, 535, A8
Bingert, S., & Peter, H. 2011, A&A, 530, A112
Brooks, D. H., & Warren, H. P. 2006, in Proc. SOHO-17: 10 Years of SOHO and Beyond, ed. H. Lacoste & L. Ouwehand (ESA-SP 617; Noordwijk: ESA)
Carlsson, M., Hansteen, V. H., & Gudiksen, B. V. 2010, MmSAI, 81, 582
Craig, I. J. D., McClymont, A. N., & Underwood, J. H. 1978, A&A, 70, 1
De Groof, A., Bastiaensen, C., Müller, D. A. N., Berghmans, D., & Poedts, S. 2005, A&A, 443, 319
De Groof, A., Berghmans, D., van Driel-Gesztelyi, L., & Poedts, S. 2004, A&A, 415, 1141
Démoulin, P., van Driel-Gesztelyi, L., Mandrini, C. H., Klimchuk, J. A., & Harra, L. 2003, ApJ, 586, 592
Dere, K. P., Landi, E., Mason, H. E., Monsignori Fossi, B. C., & Young, P. R. 1997, A&AS, 125, 149
Dere, K. P., Landi, E., Young, P. R., Del Zanna, G., & Mason, H. E. 2009, A&A, 498, 915
Fang, X., Xia, C., & Keppens, R. 2013, ApJL, 771, L29
Fischbacher, G. A., Loch, S. D., & Summers, H. P. 2002, A&A, 389, 295
Froment, C., Auchére, F., Bocchialini, K., et al. 2015, ApJ, 807, 158
Gilbert, H., Kilper, G., Alexander, D., & Kucera, T. 2011, ApJ, 727, 25
Gudiksen, B. V., & Nordlund, A. 2005a, ApJ, 618, 1020
Gudiksen, B. V., & Nordlund, A. 2005b, ApJ, 618, 1031
Hansteen, V. H., Carlsson, M., & Gudiksen, B. 2007, in ASP Conf. Ser. 368, The Physics of Chromospheric Plasmas, ed. P. Heinzel, I. Dorotovič & R. J. Rutten (San Francisco, CA: ASP), 107
Heinzel, P., Schmieder, B., Farnik, F., et al. 2008, ApJ, 686, 1383
Hood, A. W., & Priest, E. R. 1979, A&A, 77, 233
Karpen, J. T., Antiochos, S. K., & Klimchuk, J. A. 2006, ApJ, 637, 531
Karpen, J. T., Tanner, S. E. M., Antiochos, S. K., & DeVore, C. R. 2005, ApJ, 635, 1319
Klimchuk, J. A. 2006, SoPh, 234, 41
Klimchuk, J. A. 2009, in ASP Conf. Ser. 415, Proc. Second *Hinode* Science Meeting, Beyond Discovery—Toward Understanding, ed. B. Lites et al. (San Francisco, CA: ASP), 221
Klimchuk, J. A., Karpen, J. T., & Antiochos, S. 2010, ApJ, 714, 1239
Kuin, N. P. M., & Martens, P. C. H. 1982, A&A, 108, L1
Landi, E., & Reale, F. 2013, ApJ, 772, 71
Landi, E., Young, P. R., Dere, K. P., Del Zanna, G., & Mason, H. E. 2013, ApJ, 763, 86
Lenz, D. D., Deluca, E. E., Golub, L., Rosner, R., & Bookbinder, J. A. 1999, ApJL, 517, L155
Lionello, R., Linker, J. A., & Mikić, Z. 2009, ApJ, 690, 902
Lionello, R., Winebarger, A. R., Mok, Y., Linker, J. A., & Mikić, Z. 2013, ApJ, 773, 134
Luna, M., Karpen, J. T., & DeVore, C. R. 2012, ApJ, 746, 30
Lundquist, L. L., Fisher, G. H., & McTiernan, J. M. 2008a, ApJS, 179, 509
Lundquist, L. L., Fisher, G. H., McTiernan, J. M., & Régnier, S. 2004, Proc. SOHO 15 Workshop, Coronal Heating, ed. R. W. Walsh et al. (ESA-SP 575; Paris: ESA), 306
Lundquist, L. L., Fisher, G. H., Metcalf, T. R., Leka, K. D., & McTiernan, J. M. 2008b, ApJ, 689, 1388
Martens, P. C. H., & Kuin, N. P. M. 1983, A&A, 123, 216
Mendoza-Briceño, C. A., Sigalotti, L. D. G., & Erdélyi, R. 2005, ApJ, 624, 1080
Mikić, Z., Lionello, R., Mok, Y., Linker, J. A., & Winebarger, A. R. 2013, ApJ, 773, 94
Mok, Y., Lionello, R., Mikić, Z., & Linker, J. A. 2005, ApJ, 621, 1098
Mok, Y., Mikić, Z., Lionello, R., & Linker, J. A. 2008, ApJL, 679, L161
Müller, D. A. N., De Groof, A., Hansteen, V. H., & Peter, H. 2005, A&A, 436, 1067
Müller, D. A. N., Hansteen, V. H., & Peter, H. 2003, A&A, 411, 605
Müller, D. A. N., Peter, H., & Hansteen, V. H. 2004, A&A, 424, 289
Peter, H., & Bingert, S. 2013, A&A, 548, A1
Peter, H., Bingert, S., & Kamio, S. 2012, A&A, 537, A152
Rappazzo, A. F., Velli, M., Einaudi, G., & Dahburg, R. B. 2007, ApJL, 657, L47
Rappazzo, A. F., Velli, M., Einaudi, G., & Dahburg, R. B. 2008, ApJ, 677, 1348
Rosner, R., Tucker, W. H., & Vaiana, G. S. 1978, ApJ, 220, 643
Schrijver, C. J., DeRosa, M. L., Metcalf, T. R., et al. 2006, SoPh, 235, 161
Schrijver, C. J., Sandman, A. W., DeRosa, M. L., & Aschwanden, M. J. 2004, BAAS, 36, 826
Schmelz, J. T., Reames, D. V., von Steiger, R., & Basu, S. 2012, ApJ, 755, 33
Schrijver, C. J., van den Oord, G. H. J., & Mewe, R. 1994, A&A, 289, L23
Serio, S., Peres, G., Vaiana, G. S., Golub, L., & Rosner, R. 1981, ApJ, 243, 288
Vesecky, J. F., Antiochos, S. K., & Underwood, J. H. 1979, ApJ, 233, 987
Warren, H. P., & Winebarger, A. R. 2006, ApJ, 645, 711
Winebarger, A. R., Lionello, R., Mok, Y., Linker, J. A., & Mikić, Z. 2014, ApJ, 795, 138
Winebarger, A. R., Warren, H. P., & Mariska, J. T. 2003, ApJ, 587, 439
Wood, K., & Raymond, J. 2000, ApJ, 540, 563
Xia, C., Chen, P. F., Keppens, R., & van Marle, A. J. 2011, ApJ, 737, 27